

# Lattice Relaxation and Charge-Transfer Optical Transitions Due to Self-Trapped Holes in Non-Stoichiometric $\text{LaMnO}_3$ Crystal

N. N. Kovaleva,<sup>1,2,\*</sup> J. L. Gavartin,<sup>2</sup> A. L. Shluger,<sup>2</sup> A. V. Boris,<sup>1,3</sup> and A. M. Stoneham<sup>2</sup>

<sup>1</sup>*Institute of Solid State Physics, Russian Academy of Sciences, Chernogolovka, Moscow distr., 142432 RUSSIA*

<sup>2</sup>*University College London, Gower Street, London WC1E 6BT, UK*

<sup>3</sup>*Max-Planck-Institut für Festkörperforschung, Heisenbergstr. 1, 70569 Stuttgart, Germany*

(Dated: October 25, 2018)

We explore the role of electronic and ionic polarisation energies in the physics of the "colossal" magnetoresistive (CMR) materials. We use the Mott-Littleton approach to evaluate polarisation energies in  $\text{LaMnO}_3$  lattice associated with holes localized on both  $\text{Mn}^{3+}$  cation and  $\text{O}^{2-}$  anion. The full (electronic and ionic) lattice relaxation energy for a hole localized at the O-site is estimated as 2.4 eV which is appreciably greater than that of 0.8 eV for a hole localized at the Mn-site, indicating on the strong electron-phonon interaction in the former case. The ionic relaxation around the localized holes differs for anion and cation holes. That associated with  $\text{Mn}^{4+}$  is approximately isotropic, whereas ionic displacements around  $\text{O}^-$  holes show axial symmetry, the axis being directed towards the apical oxygens.

Using a Born-Haber cycle we examine thermal and optical energies of the hole formation associated with electron ionization from  $\text{Mn}^{3+}$ ,  $\text{O}^{2-}$  and  $\text{La}^{3+}$  ions in  $\text{LaMnO}_3$  lattice. For these calculations we derive a phenomenological value for the second electron affinity of oxygen in  $\text{LaMnO}_3$  lattice by matching the optical energies of  $\text{La}^{4+}$  and  $\text{O}^-$  hole formation with maxima of binding energies in the experimental photoemission spectra. The calculated thermal energies predict that the electronic hole is marginally more stable in the  $\text{Mn}^{4+}$  state in  $\text{LaMnO}_3$  host lattice, but the energy of a hole in the  $\text{O}^-$  state is only higher by a small amount, 0.75 eV, rather suggesting that both possibilities should be treated seriously.

We examine the energies of a number of fundamental optical transitions, as well as those involving self-trapped holes of  $\text{Mn}^{4+}$  and  $\text{O}^-$  in  $\text{LaMnO}_3$  lattice. The reasonable agreement with experiment of our predicted energies, linewidths and oscillator strengths leads us to plausible assignments of the optical bands observed. We deduce that the optical band near 5 eV is associated with  $\text{O}(2p) - \text{Mn}(3d)$  transition of charge-transfer character, whereas the band near 2.3 eV is rather associated with the presence of  $\text{Mn}^{4+}$  and/or  $\text{O}^-$  self-trapped holes in non-stoichiometric  $\text{LaMnO}_3$  compound.

PACS numbers: 75.30.Vn, 71.55.Ht, 78.40.Ha

## I. INTRODUCTION

The striking behaviour of the CMR oxides of  $\text{R}_{1-x}\text{A}_x\text{MnO}_3$  (R: trivalent rare-earth ions, A: divalent alkaline-earth ions,  $0.2 \leq x \leq 0.5$ ) arises from the interplay of several distinct energy terms: magnetic interactions, electronic band structure energies, crystal field splittings, vibrational energies and electron lattice coupling, including small polaron ideas and the Jahn-Teller (JT) effect. Understanding this behaviour has been helped very greatly by the use of models to map the various regimes of behaviour [1]. The experimental evidence [2] suggests that manganites are doped charge-transfer insulators having  $\text{O}(2p)$  holes as the current carriers rather than  $\text{Mn}^{3+}$  (3d) electrons. However, whether holes reside on O- and/or Mn- sites is still the subject of controversy. Some of the models of polarisation and vibration in CMR systems make major approximations, such as a single vibrational frequency (Einstein model) or rigid, unpolarizable ions. These simplifications are known to give seriously inadequate results, both quantitatively and qualitatively. For example, for the charge-transfer (CT) transitions of the zinc vacancy centre  $\text{V}^-$  in  $\text{ZnSe}$ , optical spectroscopy [3] allows one to obtain the key relaxation and tunnelling energies. But these values, in the simple one frequency, rigid-ion, model are inconsistent with the observed localization of the charge on a single Se neighbour to the vacancy [4]. However, if one goes to a general model at the harmonic and dipole approximation level, namely the shell model, there is both consistency and good agreement with experiment. What the shell model [5, 6] does which is significant is, first, to separate the ionic and electronic polarisations properly, so that phonons are predicted well and polarisation at the atomic scale is well reproduced. Secondly, the shell model recognizes that the local environment affects the polarisability of ions through short-range repulsive forces. As a result, the shell model provides a strong

---

\*Electronic address: nkovalev@issp.ac.ru

framework for understanding energies, which are dominated by polarisation and distortion. Such energies include those describing small polarons [3-5] and optical CT transitions (as considered for MgO [7] and  $V^-$  centres in ZnSe [4]). The shell model has also been used extensively in studies of defect energetics and non-stoichiometry in oxides [8]. Its considerable quantitative success arises largely because it provides such an accurate description of the large polarisation energies.

It is helpful to recognize the orders of magnitude of the several energy terms for CMR oxides. Obviously, a small energy does not mean that the particular energy is unimportant, but a small value often means that very simple ideas for those terms are sufficient when examining phenomena dominated by large energies. Typical magnitudes are these:

CMR instability energy of an electron in an external field of 10 T	0.001 eV ( $\sim \mu gH$ ),
magnetic exchange (from $kT_N$ , $T_N$ being the Neel temperature)	0.01 eV,
energy of non-cubic structural deformation of $\text{LaMnO}_3$ cell	$\leq 0.4$ eV,
Jahn-Teller energy (from largest known JT energies)	$\leq 0.4$ eV,
crystal field splitting energies (from data on many systems)	1 eV typical,
polarisation energies (net charge $\pm e$ )	5 to 10 eV,
free ion ionisation potentials	Tens of eV,
Madelung energies (fully ionic models)	Tens of eV.

In this paper we shall be concerned mainly with the polarisation energies, for which the large energy terms are dominant. We shall only discuss Jahn-Teller and crystal field (CF) energies in simple terms, although we remark that one-frequency models of the JT effect will also lead to inconsistencies.

We apply the shell model calculations to look specifically at energies associated with the localized holes of  $\text{Mn}^{4+}$  and  $\text{O}^-$  in non-stoichiometric or slightly doped "parent"  $\text{LaMnO}_3$  compound. Using this model, we address some of the issues in physics of CMR systems for which the polarisation energies are crucial. First, we calculate the electronic and ionic polarisation energies due to holes localized on  $\text{Mn}^{3+}$  and  $\text{O}^{2-}$  ions in order to estimate the key polaron energies and examine the controversial question as to whether holes reside at Mn- or O-sites in  $\text{LaMnO}_3$  lattice. Second, we estimate the energies of the main CT transitions including  $\text{Mn}^{4+}$  and  $\text{O}^-$  species, which determine specific transport properties of doped CMR materials. We analyze their contribution to the optical conductivity in the non-stoichiometric  $\text{LaMnO}_3$  crystal and make the assignment of the bands in the optical conductivity spectrum more clear-cut.

## II. DESCRIPTION OF $\text{LaMnO}_3$ SYSTEM AND SHELL MODEL APPROXIMATION

Many of the CMR materials are hole-doped systems of perovskite manganites of the form  $\text{La}_{1-x}\text{A}_x\text{MnO}_3$ . Their properties are intimately related to those of the "parent" compound ( $x=0$ ).  $\text{LaMnO}_3$  is an A-type antiferromagnet below the  $T_N \simeq 140$  K, in which the  $\text{MnO}_2$  ferromagnetic layers are stacked along the c-axis with alternating spin directions. The structure of the perovskite manganites can be clearly understood starting from the simple cubic perovskite structure ( $Pm\bar{3}m$ ). The idealized cubic structure of  $\text{LaMnO}_3$  featuring a chain of the corner-sharing  $\text{MnO}_6$  octahedra is presented in Figure 1. The  $\text{Mn}^{3+}$  ion with the  $3d^4$  electronic configuration is known to exhibit a large Jahn-Teller effect in other systems [9]. Therefore it is natural to assume that the JT instability of the  $\text{Mn}^{3+}$  ion can contribute to an orthorhombic distortion of the perovskite structure of  $Pnma$  symmetry in  $\text{LaMnO}_3$  crystal. The orthorhombic structure can be obtained from the cubic perovskite structure by the two consequent and coordinated rotations of the  $\text{MnO}_6$  octahedra around the  $[010]$  and  $[101]$  directions, as shown in Figure 1. Another possible contribution to the observed distortion from cubic symmetry in  $\text{LaMnO}_3$  could be attributed to an atomic size mismatch: the sum of the Mn-O layer ionic radii,  $r_{\text{Mn}} + r_{\text{O}}$ , does not match that of the La-O layer,  $(r_{\text{La}} + r_{\text{O}})/\sqrt{2}$ , in the right way for a stable cubic structure. Size mismatch effect is known to be a common reason for distortions in different perovskite oxides. Our shell model calculations performed for  $\text{LaMnO}_3$   $Pnma$  structure point out that the orthorhombic distortions experimentally observed at low temperatures could not be caused by simply lattice mismatch effect (which, in principle, must be properly described in the framework of the shell model approximation), but rather caused by the both effects, with a comparative contribution from the JT effect. Some special efforts should be undertaken to account for the JT effect empirically in the framework of the shell model. We perform the shell model calculations for the cubic perovskite structure (Figure 1) in the present work. This approximation seems to be mostly relevant to the non-magnetic quasicubic perovskite structure of  $\text{LaMnO}_3$  crystal experimentally observed at high temperatures  $T \geq 400$  K  $> T_N \simeq 140$  K. We suggest our modeling of the cubic perovskite structure provides a reasonable model as we are mainly interested to estimate the key polarization energies associated with polaron-type charge carriers in the high-temperature insulating quasicubic phase of the CMR lattices.

We model the  $\text{LaMnO}_3$  system using methods based on the shell model and Mott-Littleton approach which have successfully been applied to study properties of a wide range of oxides (including transition metal oxides), halides and

other systems [10, 11]. The calculations are performed using the GULP code [12]. In the shell model [5] the lattice is considered as an assembly of polarizable ions, represented by massive point cores and massless shells coupled by isotropic harmonic forces. Interacting potential includes contributions from Coulomb, polarization and short-range interactions. We adopt a fully ionic model (with formal charges of ions in the  $\text{LaMnO}_3$  lattice:  $\text{La}^{3+}$ ,  $\text{Mn}^{3+}$ , and  $\text{O}^{2-}$ ). This is less restrictive than one might think, since a parallel covalent description is possible [13]. The sum of the core and shell charges is equal to the formal charge of the ion in the lattice. The core and shell charges and the spring constant of each ion are parameters of the model. The electronic polarisation of the ions is represented by the displacement of their shells relative to the cores in the dipole approximation. The lattice distortion is simulated by the core displacements from their lattice site positions.

In our model cations are treated unpolarizable and short-range interactions between the relatively small cations (core-core) are ignored. The short-range potentials used for the shell-shell (oxygen-oxygen) and core-shell (metal-oxygen) interactions are of the Buckingham form:

$$V_{ij} = A_{ij} \exp(-r/\rho_{ij}) - C_{ij}/r^6 \quad (1)$$

The parameters of both repulsive and attractive components of Buckingham potential for shell-shell ( $\text{O}^{2-} : \text{O}^{2-}$ ) interactions used in this work are obtained in ref. [14] and presented in Table I, (a). The Buckingham parameters for the core-shell  $\text{Mn}^{3+} : \text{O}^{2-}$  and  $\text{La}^{3+} : \text{O}^{2-}$  interactions were fitted in this work using the experimental data including the lattice parameter, the static and high-frequency dielectric constants, and the frequencies of the transverse optical phonons in  $\text{LaMnO}_3$  crystal [15]. The dielectric constants are especially important if one wishes to predict polarisation energies accurately. We have not found out an experimental value of the static dielectric constant of  $\text{LaMnO}_3$  in the literature. We are grateful to T. Arima and Y. Tokura [16] for sending us the experimental data on the reflectivity spectra of  $\text{LaMnO}_3$  measured at room temperature and reported in ref. [15]. The experimental value of the static dielectric constant  $\epsilon_0 \approx 18 \pm 2$  was derived from these data in the present work by the Kramers-Kronig analysis, and further used in the fitting procedure. The parameters fitted for  $\text{LaMnO}_3$  ( $Pm\bar{3}m$ ) in ref. [17] (see Table I, (b)) were used as the starting values for the core-shell  $\text{La}^{3+} : \text{O}^{2-}$  and  $\text{Mn}^{3+} : \text{O}^{2-}$  short-range interaction potentials. The oxygen shell charge was taken of  $-2.48 |e|$  and the shell-core spring constant  $k$  was chosen to give the correct value for the static dielectric constant  $\epsilon_0$ .

The final values of our shell-model parameters are presented in Table I, (a). The calculated and experimental properties of  $\text{LaMnO}_3$  ( $Pm\bar{3}m$ ) are summarized in Table II. One can see that both sets of parameters (Table I, (a,b)) give close values for the lattice parameter and cohesive energy, however, our parameters at the same time give results close to the static and high-frequency dielectric constants. The value of the static dielectric constant calculated with the parameters of ref. [17] is much higher than that derived from the experimental reflectivity spectra. Our model also agrees well with the experimental values of the transverse optical phonon energies [15]. The phonon bands obtained in our calculations correlate well with those observed with higher oscillator strengths. In particular, the predicted phonon energies agree well for the La-external ( $\omega_{TO_1}$ ), Mn-O-Mn bending mode ( $\omega_{TO_2}$ ) and Mn-O stretching mode ( $\omega_{TO_3}$ ) for the quasicubic perovskite structure of the strongly doped perovskite manganite system  $\text{La}_{0.67}\text{Ca}_{0.33}\text{MnO}_3$  [18, 19].

We have also tested yet another set of short-range pair potentials which are different for Mn ion in different valence states  $\text{Mn}^{2+}$ ,  $\text{Mn}^{3+}$ , and  $\text{Mn}^{4+}$ . They were obtained by fitting the equilibrium structures of several oxide compounds, such as  $\text{MnO}$ ,  $\text{LaMnO}_3$ , and  $\text{Ca}_2\text{MnO}_4$  [20]. We tested pair-potentials for  $\text{Mn}^{4+}$  and  $\text{Mn}^{3+}$  from this set, presented in Table I, (c). These parameters also give good results (see the set of values (c) in Table II) for the lattice parameter and the dielectric constants, but are less successful in predicting the optical phonon frequencies. As will be shown below, both these and our parameters give similar values for the calculated properties of polarons in these crystals validating the correctness of the shell model approach.

We apply then the shell model parameters to estimate key defect energies using the well-known Mott-Littleton method (see ref. [11] for more detailed description). It is based on the concept that the total energy of the crystal lattice containing defect is minimized by a relaxation of the ions surrounding the defect, and this relaxation decreases fairly rapidly for distances away from the defect. In these calculations, the crystal is divided into three regions: an inner spherical region I, containing the defect and its immediate surroundings, an intermediate finite region II, which is created to link properly region I and an outer infinite region III, which responds as a dielectric continuum. The finite regions I and II are embedded in the infinite region III. The typical radii of regions I and II used in our calculations were 10 and 25 Å, respectively. We considered an electronic hole located in the centre of region I, which is the most perturbed. The displacements of cores and shells in this region are calculated explicitly. In intermediate region II the ions are also treated in the shell model, but their displacements and polarisations are derived from the dielectric continuum approximation. The system total energy is minimized (the preset accuracy was of 0.01 eV) with respect to the positions of all cores and shells in regions I and II in the potential produced by the polarized region III.

The Mott-Littleton method is especially valuable to estimate key polaron energies because the long-range polarization fields are treated properly; many other methods (such as cluster methods or periodic cell methods) treat these significant terms badly.

### III. ELECTRONIC HOLES IN $\text{LaMnO}_3$

#### A. Relaxation energies of the localized holes in $\text{LaMnO}_3$

We study possible hole localisation (self-trapping) on  $\text{Mn}^{3+}$  and on  $\text{O}^{2-}$  ions in slightly hole-doped or non-stoichiometric  $\text{LaMnO}_3$  crystal. Theoretical predictions of electron charge carrier self-trapping in ideal lattice are based on calculations of the so-called self-trapping energy [10], which is the difference between the localisation and relaxation energies. The first of these terms is basically an increase in the hole (electron) kinetic energy due to its localisation on a finite number of lattice sites from a completely delocalized state. The second is the energy gain due to the lattice polarisation by the localized charge. They represent a very delicate balance of large terms which in many cases differ by only 0.1 eV. The calculation of the localisation energy, especially in complex crystals, is the most difficult part of study of electron charge carrier self-trapping [10], and needs accurate electronic structure calculations not within the scope of this work. Our aim is rather to compare the relaxation energies for the hole localisation in two different sublattices of the same crystal. These energies are indicative of the strength of the electron-phonon interaction and their difference can suggest whether there are major differences in hole trapping in one of the sublattices.

The process of the hole formation can be generally seen as the ionisation of the *in-crystal* ion with an electron being taken out of the crystal and put on the vacuum level. The energy required in this process (hole formation energy,  $E_h^\alpha$ ,  $\alpha = \text{Mn, O, La}$ ) is the work done against the *in-crystal* ionic core potential,  $I^\alpha$ , and the crystalline electrostatic potential,  $U_M^\alpha$ , less then energy gain due to the lattice polarisation effects,  $R^\alpha$

$$E_h^\alpha = I^\alpha + U_M^\alpha + R^\alpha. \quad (2)$$

To assess the extent of the lattice perturbation by the hole localisation and calculate the hole relaxation energy, it is useful to distinguish the 'electronic' and 'ionic' terms in the polarisation energy. The former term, which we will call  $R_{opt}^\alpha$ , is due to the 'electronic' polarisation of ions by the momentarily localized hole, which in our method is represented by the displacements of shells with respect to the cores which are fixed at their perfect crystal positions. It takes into account the lattice response after e.g. Franck-Condon photoionisation. The lattice distortion term due to displacements of cores and related adjustment of shells after complete lattice relaxation, denoted as  $\Delta R_{th}^\alpha$ , is the difference between the full polarisation energy,  $R^\alpha$ , and the  $R_{opt}^\alpha$

$$\Delta R_{th}^\alpha = R^\alpha - R_{opt}^\alpha. \quad (3)$$

It represents the hole relaxation energy. If this energy exceeds the localisation energy, i.e. the kinetic energy rise due to complete hole localisation on this site, then one can talk about the hole being self-trapped on this site. Given this assumption, Eq. (2) takes the form

$$E_h^\alpha = I^\alpha + U_M^\alpha + R_{opt}^\alpha + \Delta R_{th}^\alpha. \quad (4)$$

The shell-model Mott-Littleton calculations give the cumulative energy of the second and third term,  $S_{opt}^\alpha$ , or of the last three terms,  $S_{th}^\alpha$ , in Eq. (4) depending whether both shells and cores or shells only were allowed to relax. It is sensible, however, to evaluate these terms separately. This can be rigorously done by calculating independently the on-site electrostatic potential  $U_M^\alpha$  within the periodic model and using the definition introduced in Eq. (3). The values of  $S_{opt}^\alpha$ ,  $S_{th}^\alpha$  and the calculated terms of  $U_M^\alpha$ ,  $R_{opt}^\alpha$ , and  $\Delta R_{th}^\alpha$  are summarized in Table III.

It follows from these calculations that there is a large difference in the lattice relaxation energies for  $\text{O}^-$  and  $\text{Mn}^{4+}$  holes. The lattice relaxation energy,  $-\Delta R_{th}^\alpha$ , caused by the hole localisation at the O-site (2.38 eV) appears to be significantly larger than that for the hole localized at the Mn-site (0.83 eV), as shown in Table III, (a). This indicates on the strong electron-phonon interaction in the case of the hole localized at the O-site and could suggest that the hole trapping is more preferential in the oxygen sublattice. However, the width of the Mn(3d) subband in the density of states, which determines the hole localisation energy, is much narrower than that of the O(2p) related subband [21]. Therefore without a much fuller electronic structure calculation of the localisation energy it is impossible to draw any final conclusion as to in which sublattice the holes could be localized.

One experimental test could involve the analysis of local vibrations due to the hole localisation. It can be facilitated by the qualitative difference in the lattice relaxation around the two centres which is clearly seen in Figures 2 and 3. The fully relaxed configuration of the ions surrounding the  $\text{Mn}^{4+}$  electronic hole defect (see Figure 2) corresponds to

the positions of cores in region I which have appreciable displacements ( $\geq 0.004$  Å) from their perfect lattice sites. The cores of the six nearest neighbour oxygen ions are displaced symmetrically by about 0.1 Å towards the  $\text{Mn}^{4+}$  ion carrying the hole. The rest of the lattice relaxation comprises small displacements of Mn and La ions (of about 0.01 and 0.004 Å, respectively) out from the  $\text{Mn}^{4+}$  hole center.

By contrast, the ionic relaxation around the  $\text{O}^-$  hole center has the axial symmetry, with the largest lattice displacements of the nearby Mn ions (of about 0.21 Å) along the axis away from the  $\text{O}^-$  hole center (see Figure 3). These displacements cause the next two apical oxygen ions along the axis to move away from the  $\text{O}^-$  hole center by about 0.1 Å. The equatorial oxygen ions in the octahedron relax towards the hole center by about 0.03 Å. In-plane La ions also show appreciable displacements away from the  $\text{O}^-$  hole center. The qualitative difference in the symmetry of the lattice relaxation around the two centres implies the difference in the local vibrational modes, which can be used for experimental probing of hole localisation in  $\text{LaMnO}_3$ .

### B. Photoemission spectra and "in-crystal" ionisation potentials in $\text{LaMnO}_3$ . Formation energies of the localized holes in $\text{LaMnO}_3$ crystal

In order to evaluate the hole formation energy, we need to estimate the values of the unknown *in-crystal* ionisation energies,  $I^\alpha$ . We suggest estimating the ionisation potentials from the experimental photoemission spectroscopy (PES) data, which can be directly related to our calculations. PES at different excitation energies probes in principle bonding states as well as non-bonding states. The latter, being ion-in-crystal-like, can be related to the Frank-Condon energies obtained in our calculations. In order to juxtapose experimental and calculated values we need also to take into account that PES binding energy,  $E_{PES}$ , is measured with respect to sample's Fermi energy level  $E_F$ . So, we write

$$I^\alpha + U_M^\alpha + R_{opt}^\alpha = E_{PES}^\alpha + E_F. \quad (5)$$

In the PES spectra of  $\text{LaMnO}_3$  there are two main photoemission bands around 3.5 and 6 eV binding energies at  $T = 100, 200$  K for the He I ( $h\nu = 21.2$  eV) and He II ( $h\nu = 40.8$  eV) photon energies for which the O(2p) photoionisation cross-section is dominant [22]. The main maximum at 3.5 eV has been assigned primarily to the O(2p) non-bonding states, whereas the second maximum is assigned to the Mn(3d) - O(2p) bonding states and the decreasing of O(2p) character correlates with decreasing of Mn(3d) - O(2p) hybridization strength. For higher energies with He II PES study the Mn(3d)/O(2p) cross-section ratio increases and a feature near 2.7 eV appears [22]. At high photon energies, 500 eV, and  $T = 280$  K, the band at 3.5 eV is not clear evident, but the band at 2.7 eV becomes dominant over the band at 6 eV, which stands for maximum contribution from Mn(3d)  $3t_{2g}$  states at 2.7 eV binding energy [23]. The crystal field (CF) splitting between Mn(3d)  $3t_{2g}$  and  $e_g$  states in  $\text{LaMnO}_3$  has been estimated to be about  $\Delta_{CF} \simeq 1.5$  eV from the PES study [23]. The peak at 17 eV has been assigned to the La(5p) states [23].

So, in accordance with the dominant contributions to the PES spectra of  $\text{LaMnO}_3$  [22, 23], we assign the following values  $E_{PES}^O \simeq 3.5$  eV,  $E_{PES}^{La} \simeq 17.0$  eV, and  $E_{PES}^{Mn} \simeq 1.2$  eV, suggesting the process of Mn hole formation is associated with electron photoionisation from  $e_g$  level. These maxima in the PES spectra correlate well with the maxima in the density of states (DOS) for O(2p) and Mn(3d)  $e_g$  valence bands in  $\text{LaMnO}_3$  calculated within the local spin density approximation (LSDA) [21]. The corresponding schematic representation of the band structure in accordance with the assigned maxima of binding energies in the PES spectra [22, 23] in the scale of energies related to the crystal Fermi level  $E_F$  is shown in Figure 4. The gap in the  $e_g$  electron band opened at the  $E_F$  due to the lattice distortion (the Jahn-Teller effect and/or lattice mismatch effect) is shown in accordance with the CF splitting PES data [23]. The relevant electron excitations from the Mn(3d)  $e_g$ , O(2p) and La(5p) valence band levels are schematically shown by arrows. The corresponding PES energies,  $E_{PES}^\alpha$ , are summarized in Table III.

Having assigned the  $E_{PES}^\alpha$  energies we now proceed with the evaluation of the hole formation energies  $E_h^\alpha$ . First, we obtain the crystal Fermi energy by using Eq. (5) and data for the La ion. We assume that the electronic density of the closed-shell  $\text{La}^{3+}$  ion is not significantly deformed by the crystalline field, so *in-crystal* ionisation energy,  $I^{La}$ , can be plausibly estimated by the forth standard ionisation potential of a free La atom [24], presented in Table III. This approximation is consistent with the full ionic charges adopted in our shell model parameterization. We note that the approximation of a free cation just made, is shown to be reliable only for the closed-shell cations. This gives  $E_F \simeq 1.36$  eV for the Fermi energy of  $\text{LaMnO}_3$  crystal.

The situation is more complicated in the case of manganese and oxygen. The  $\text{Mn}^{3+}$  ion has non-closed 3d shell with four electrons in it, so we expect that the *in-crystal* ionisation energy,  $I^{Mn}$ , could differ from the fourth ionisation potential of a free Mn atom. The  $\text{O}^{2-}$  ion is only stabilized by the crystalline field, thus it has a negative ionisation potential which can not be defined in a non-speculative way. Using the Mn(3d) and O(2p) related maxima in the PES spectra,  $E_{PES}^\alpha$ , and the obtained value for  $E_F \simeq 1.36$  eV, we can now estimate the effective ionisation energies,  $I^\alpha$ , for manganese and oxygen in  $\text{LaMnO}_3$  crystal from Eq. (5). These values are presented in Table III, the free

metal ionisation potentials [24] are given for comparison in brackets. The  $O^{2-}$  *in-crystal* ionisation potential  $I^O$  (negative electron affinity of  $O^-$ ) is estimated thereby to be -13.91 eV. This absolute value is within the limits of  $O^-$  electron affinities calculated for many oxide compounds in ref. [25] using an embedded cluster *ab-initio* method. Those calculations predicted 10.6 eV for MgO and 12.9 eV for  $ThO_2$ . Taking into account the semi-empirical nature of our calculations we find this agreement quite good.

The optical and thermal energies of hole formation,  $E_h^\alpha(opt)$  and  $E_h^\alpha(th)$ , are calculated using these effective values of the *in-crystal* ionisation energies in accordance with Eq. (4) and presented in Table III. Taking into account the CF splitting effect we have found out that the electronic hole is marginally more stable at the Mn-site than at the O-site in the  $LaMnO_3$  lattice, but the energy difference between the thermal energies of the hole formation,  $E_h^\alpha(th)$ , is too small (0.75 eV). This result rather suggests that both possibilities should be treated seriously. That is, providing the balance between the localisation and relaxation energies favours the possibilities for the hole self-trapping at the Mn- and O-sites, the electronic hole in  $LaMnO_3$  will be likely localized on the manganese, or on both oxygen anion and transition metal cation, rather than on the oxygen ion alone.

In order to assess the accuracy of the calculated energies of the hole formation and lattice relaxation we need to discuss the following issue. This issue concerns the pair potentials used in these calculations. The energies presented in Table III, (a) were obtained using the pair potentials listed in Table I, (a). To check the robustness of our results, we repeated the same calculations using the potentials from R. Grimes and D. Bradfield [20], which give close values for the dielectric constants in  $LaMnO_3$  (see Table II, (c)), but were specially optimized to treat different  $Mn^{3+}$  and  $Mn^{4+}$  charge states. The calculated values of formation and polarisation energies for the localized holes  $Mn^{4+}$ ,  $O^-$  and  $La^{4+}$  and the energies deduced in Eq. (4) using these pair-potentials are presented in Table III, (c). These calculations demonstrated that the hole relaxation energy of  $Mn^{4+}$  is decreased by 0.16 eV if we account for the change in the short-range potentials caused by the change of the Mn charge state. Comparing with our results, we can see good coincidence for the similar values and for the thermal and optical energies of hole formation.

#### IV. OPTICAL CHARGE-TRANSFER TRANSITIONS IN $LaMnO_3$

Polaronic-type electron charge carriers mostly determine specific transport properties of CMR materials in their high-temperature insulating paramagnetic phase, which are always associated with photo-induced charge-transfer (CT) transitions. In hole-doped systems of perovskite manganites of  $R_{1-x}A_xMnO_3$  the main important CT transitions associated with localized charge carriers will be apparently those involving  $Mn^{4+}$  and  $O^-$  self-trapped holes. In this section using the derived values of the *in-crystal* ionisation energies we calculate energies of the main CT transitions suggesting that holes could be localized at the Mn- or O-sites. We analyze the contribution of these CT transitions to the experimental optical conductivity in non-stoichiometric or slightly hole-doped  $LaMnO_3$  crystals to make the assignment of the bands in the optical conductivity spectrum more clear-cut and to verify our shell model approach. Now we proceed with brief analysis of the optical conductivity spectra.

##### A. Analysis of the optical conductivity spectra in $LaMnO_3$

The room temperature optical conductivity spectrum of  $LaMnO_3$  measured in [15] is shown by solid curve 1 in Figure 5, (a) in the spectral region 0 to 8 eV (reproduced from the original data with a permission of T. Arima and Y. Tokura [15, 16]). This spectrum is very similar to that measured by Okimoto *et al.* at  $T = 9$  K [26]. It reveals the optical gap near 1.3 eV and includes several broad absorption bands with maxima at  $\sim 2.3$ , 5 and 9 eV. The gap is assumed to be of the charge-transfer type [15]. The first transition at  $\sim 2.3$  eV has been suggested to be of the  $O(2p) - Mn(3d)$  character. The band at  $\sim 5$  eV is thought to be due to the excitations to a higher-lying Mn 3d  $e_g$  antiparallel spin configuration, separated by a Hund's rule coupling energy. The wide band observed around 9 eV in the optical conductivity spectrum is assigned to the  $O(2p) - La(5d)$  interband optical transition [15].

The optical spectra measured in hole-doped manganese oxides show striking changes over a wide photon region (0 to 6 eV) as the temperature and doping concentration change. In  $La_{1-x}Sr_xMnO_3$  system, with increasing doping concentration ( $x = 0$  to 0.3,  $T = 9$  K, [26]), the excitations around 2.3 and 5 eV shift appreciably to lower energies. However, the principal changes take place in the low-energy mid-infrared spectral region stemming from the filling of the gap because of the hole doping. In the insulating paramagnetic phase of hole-doped manganites there are two features clearly observed in the experimental mid-infrared optical conductivity, around 0.6 eV [18, 26] and around 1.2 - 1.5 eV [27, 28]. The optical band at  $\sim 0.6$  eV seems to be associated with polaronic-type charge carriers in doped CMR manganites, and the consistent value of activation energy of  $\sim 0.15$  eV was measured for the hopping conductivity in the adiabatic temperature limit [29, 30]. The origin of these features is still a subject of many controversial discussions. It is well known that  $LaMnO_3$  crystal has a strongly distorted orthorhombic structure at low temperatures, which

in many works is ascribed due to strong electron-phonon interaction stemming from Jahn-Teller (JT) effect inherent for  $\text{Mn}^{3+}$  ion in the octahedral oxygen configuration. In this case the  $e_g$  bands split into two subbands, separated by the Jahn-Teller energy,  $E_{JT}$ . As the on-site  $d-d$  transitions are dipole-forbidden, these mid-infrared peaks around 0.6 and 1.2 - 1.5 eV were qualitatively explained as due to an electron transition from an occupied site  $\text{Mn}^{3+}$  to an unoccupied site  $\text{Mn}^{4+}$  and to an adjacent occupied site  $\text{Mn}^{3+}$ , respectively [1].

In a recent theoretical study of the optical conductivity spectra of 3d transition metal perovskites  $\text{LaMO}_3$  ( $M = \text{Ti} - \text{Cu}$ ) [31] using the local spin density approximation (LSDA + U) method, the authors estimated the role of the lattice distortions in the band structure calculations and concluded that the Jahn-Teller structural distortions play a crucial role in opening the optical gap in  $\text{LaMnO}_3$   $\text{Mn}(3d) e_g$  valence band. Considering the experimentally observed distorted structure of  $\text{LaMnO}_3$  crystal, the direct gap in the LSDA study has been estimated to be  $\approx 0.7$  eV, which is less than the observed optical gap ( $\approx 1.3$  eV [15, 26]). There are also some discrepancies observed at higher energies between the experimental optical conductivity in the 3d transition metal perovskites of  $\text{LaMO}_3$  and the calculated optical conductivity considering contributions from the interband and intraband transitions for the perfect lattice [31], which makes the assignment of the optical bands complicated. In addition, the contribution from the CT transitions to the optical conductivity in the non-stoichiometric lattice must be taken into account to describe satisfactorily the optical conductivity at low energies and to make the assignment of the optical bands in  $\text{LaMnO}_3$  crystal more clear-cut.

To estimate the contribution to the experimental optical conductivity of  $\text{LaMnO}_3$  crystal, shown by solid curve 1 in Figure 5, (a) from the CT transitions we have analyzed the imaginary part of the dielectric function,  $\epsilon_2(\nu)$  [15, 16]. For this purpose, we presented the  $\epsilon_2(\nu)$  spectrum, shown by solid curve 1 in Figure 5, (b), by a sum of the first three main bands with Lorentzian lineshapes

$$\epsilon_2(\nu) = \sum \nu_{pi}^2 \gamma_i \nu / [(E_i^2 - \nu^2)^2 + \gamma_i^2 \nu^2] \quad (6)$$

where  $(\nu_{pi}/E_i)^2 = f_i$  is the oscillator strength,  $\gamma_i$  is the width of the band and  $E_i$  is the resonance frequency of the  $i$ -oscillator. The three Lorentzian bands with the maxima  $E_i$  at 1.93, 4.75 and 9.07 eV and widths  $\gamma_i$  of 1.46, 2.0 and 5.1 eV, respectively, are represented by short-dashed 2, dotted 3 and long-dashed 4 curves in Figure 5, (b). The rest of the imaginary part of the dielectric function after subtraction of the Lorentzian bands is shown by light curve 5. The Lorentzian band parameters together with the estimated oscillator strengths are given in Table IV. These Lorentzian bands contribute to the experimental optical conductivity spectrum, as shown by the corresponding lines in Figure 5, (a), with more details at low energies.

## B. Calculation of charge-transfer transition energies

Using a Born-Haber cycle and the shell model we can consider both thermally assisted and optical CT processes. This can be illustrated for a hypothetical case of two ions  $X^{(m+1)+}$ ,  $Y^{(n-1)+}$  transformation into  $X^{m+}$ ,  $Y^{n+}$  in which an electron is transferred from Y to X (or a hole from X to Y):

$$X^{(m+1)+} + Y^{(n-1)+} \Rightarrow X^{m+} + Y^{n+}. \quad (7)$$

There are two basic steps: 1. Remove an electron from the *in-crystal*  $Y^{(n-1)+}$  ion to infinity, outside the crystal. 2. Add an electron from the infinity, outside the crystal, to the *in-crystal*  $X^{(m+1)+}$  ion. The steps are standard within the shell model. Whether or not shells alone, or shells and cores, are relaxed depends on which transition is being calculated. In the case of thermally assisted hopping, the shell and core positions are considered to be fully relaxed in both charge states and the transition energy is denoted  $E_{th}$ . Comparison of the two charge states gives an additional indication which species are more stable. For optical transitions, the Franck-Condon approximation is used and their energies  $E_{opt}$  are calculated on the assumption that only shells are able to relax (corresponding to full electronic polarisation), whereas the cores remain in the positions corresponding to the initial state. The major contributions into these energies come from ionisation energies,  $I_n^Y$ ,  $I_{(m+1)}^X$ , and the Madelung and polarisation terms, which cumulative energies for defect configuration corresponding the CT transition considered,  $S[X^{m+}, Y^{n+}]_{(opt,th)}$ , result from the Mott-Littleton calculations (like in Eq. 4). If the CT includes the localized hole in thermal equilibrium in the initial state (the related values in  $\text{LaMnO}_3$  lattice are presented as  $S_{th}^\alpha$  in Table III), the correspondent thermal energy for initial defect configuration,  $S[X^{(m+1)+}, Y^{(n-1)+}]_{th}$ , must be subtracted. Thus, the thermal and optical energies of the CT transitions can be calculated using the following formula

$$E_{opt} = I_n^Y - I_{m+1}^X + S[X^{m+}, Y^{n+}]_{opt} - S[X^{(m+1)+}, Y^{(n-1)+}]_{th} \quad (8)$$

$$E_{th} = I_n^Y - I_{m+1}^X + S[X^{m+}, Y^{n+}]_{th} - S[X^{(m+1)+}, Y^{(n-1)+}]_{th}. \quad (9)$$

There will clearly be some dependence on the separation of X and Y. The CT optical transitions for nearest neighbours are likely to dominate and the relevant key cases have been calculated. If X and Y are the same (symmetric) the ionisation terms cancel out, as for intervalence CT transition  $\text{Mn}^{4+} + \text{Mn}^{3+} \Rightarrow \text{Mn}^{3+} + \text{Mn}^{4+}$ . We would like to emphasize here that the calculations of CT transitions between the ions of metal Mn sublattice are more reliable because they do not depend on the difference in the Madelung potential between the two sublattices, nor on the phenomenologically deduced parameter of the  $\text{O}^{2-}$  *in-crystal* ionisation potential.

The cumulative thermal and optical energies following from the Mott-Littleton calculations,  $S_{th}$  and  $S_{opt}$ , for the CT transitions involving  $\text{Mn}^{4+}$  and  $\text{O}^-$  species, and those characterizing fundamental electronic transitions in  $\text{LaMnO}_3$  lattice, such as, Mn(3d) gap transition, O(2p) - Mn(3d), and O(2p) - La(5d) are presented in Table V by the transitions 1-3 and 4-6, respectively. To calculate the optical and thermal energies of the CT transitions we used a self-consistent set of the ionisation potentials (see Table III, (a)), derived by matching the calculated optical energies of the hole formation with the photoemission experimental energies and the standard ionisation potentials for a La free atom. We also need to estimate the third *in-crystal* ionisation potential of Mn,  $I_{III}^{Mn}$ . We suggest that it should be shifted *in-crystal* from the standard value for a Mn free atom (33.67 eV [24]) by the same value as the fourth potential of Mn (from the standard value 51.2 eV), by subtraction the crystal field (CF) splitting effect ( $\Delta_{CF} \simeq 1.5$  eV), so we calculate: *in-crystal*  $I_{III}^{Mn} = 33.67 - (51.2 - (47.41 + \Delta_{CF}/2)) = 30.63$  eV.

Taking the standard value of  $I_{III}^{La} = 19.18$  eV, the calculated optical energy of the fundamental transition of CT character O(2p) - La(5d),  $E_{opt} = I^O - I_{III}^{La} + S[\text{La}^{3+}, \text{O}^{2-}]_{opt} = 8.93$  eV (see Table V, transition 6) correlates well with the maximum of the broad band in the  $\epsilon_2$  function near 9.07 eV (long-dashed curve 4 in Figure 5, (b)). This encouraging consistency between the experimental and calculated energies let us to suggest that the earlier estimated value of  $I^O = -13.91$  eV *in-crystal* provides a reasonable value in this shell model calculations. We also calculated optical energy of the fundamental transition of CT character O(2p) - Mn(3d),  $E_{opt} = I^O - I_{III}^{Mn} + S[\text{Mn}^{3+}, \text{O}^{2-}]_{opt} = 5.61$  eV (see Table V, transition 5). We suggest that the relevant transition should correlate with the broad optical band observed in the  $\epsilon_2$  function near 4.75 eV (dotted curve 3 in Figure 5, (b)). Our calculations therefore predict transitions which appear to correlate with the maxima of the major broad-band features in the optical conductivity spectrum. The calculated optical energy for the transition between the Mn(3d) valence band and the upper Hubbard Mn(3d) band is estimated to be  $E_{opt} = I_{IV}^{Mn} - I_{III}^{Mn} + S[\text{Mn}^{3+}, \text{Mn}^{3+}]_{opt} = 3.72$  eV (see Table V, transition 4) predicting the Mott-Hubbard band gap type in  $\text{LaMnO}_3$  crystal. This value agrees well with the assigned transition experimentally observed at  $\sim 3.5$  eV in  $\text{Nd}_{0.7}\text{Sr}_{0.3}\text{MnO}_3$  [27] and at  $\sim 3.2$  eV in  $\text{La}_{0.825}\text{Sr}_{0.175}\text{MnO}_3$  [32]. A small contribution to the experimental optical conductivity can be observed around 3.7 eV in  $\text{LaMnO}_3$  crystal, as shown by light curve 5 in Figure 5, (b) resulting from our dispersion analysis.

Having assigned the fundamental electronic transitions in  $\text{LaMnO}_3$  crystal in accordance with the results of our calculations, which are also consistent with the consideration given in ref. [27], we should note that the assignment of the optical conductivity band at  $\sim 2.3$  eV still remains controversial. In the earlier study [15] this band has been associated with the fundamental CT transition of O(2p) - Mn(3d)  $e_g$  character, whereas the band at about 5 eV has been associated by the authors with the excitations to a higher-lying Mn 3d  $e_g$  antiparallel spin configuration, separated by a Hund's rule coupling energy. However, our results allow us to argue that an alternative interpretation of this transition obtained in this work can be correct. We suggest that the band at  $\sim 2.3$  eV is rather associated with the presence of  $\text{Mn}^{4+}$  and/or  $\text{O}^-$  localized holes in  $\text{LaMnO}_3$  crystal, which is known to exhibit strongly non-stoichiometric behavior with respect to oxygen content, up to 0.1 in as-grown crystal.

Indeed, if an optical band is associated with a CT transition in a crystal lattice, its maximum position,  $h\nu_{max}$ , and the half-width,  $\Delta W$ , are known to be linked by a simple formula in the high temperature limit [33]

$$h\nu_{max} = (16 \cdot (\ln 2) kT)^{-1} \Delta W^2. \quad (10)$$

We can invoke this expression to verify the CT transition character of the bands associated with photo-induced hopping conductivity of the localized charge carriers. Using this expression, estimates for  $T = 300$  K show very encouraging consistency between the half-width and the maximum energy of the first Lorentzian band (short-dashed curve 2 in Figure 5, (b), with the parameters given in Table IV): from  $\Delta W \simeq 0.73$  eV we obtain  $h\nu_{max} \simeq 1.92$  eV, which matches well the maximum position estimated to be near 1.93 eV from the dispersion analysis of the  $\epsilon_2$  function. So, this is consistent with the view that this transitions could be of CT-type, associated with the presence of localized electronic charge carriers in  $\text{LaMnO}_3$  crystal lattice.

Among these main contributions to the optical conductivity will be expected from the following CT transitions: 1) the intervalence  $\text{Mn}^{3+}/\text{Mn}^{4+}$  CT transition,  $\text{Mn}^{4+} + \text{Mn}^{3+} \Rightarrow \text{Mn}^{3+} + \text{Mn}^{4+}$ ,  $E_{opt} = S[\text{Mn}^{3+}, \text{Mn}^{4+}]_{opt} - S_{th}^{Mn} = 1.33$  eV, 2) the transition of the  $\text{O}^-$  self-trapped hole to a neighbouring manganese ion,  $\text{O}^- + \text{Mn}^{3+} \Rightarrow \text{O}^{2-} + \text{Mn}^{4+}$ ,  $E_{opt} = I_{IV}^{Mn} - I^O + S[\text{O}^-, \text{Mn}^{3+}]_{opt} - S_{th}^O = 1.43$  eV, 3) the transition of the  $\text{Mn}^{4+}$  self-trapped hole to a neighbouring oxygen ion,  $\text{Mn}^{4+} + \text{O}^{2-} \Rightarrow \text{Mn}^{3+} + \text{O}^-$ ,  $E_{opt} = I^O - I_{IV}^{Mn} + S[\text{O}^{2-}, \text{Mn}^{4+}]_{opt} - S_{th}^{Mn} = 2.98$  eV, (see transitions 1 - 3, respectively, in Table V).



Analyzing all calculated and experimental optical energies given in Table V we can conclude that the agreement is much better for those calculations not including the *in-crystal* ionisation potentials of manganese,  $I_{III}^{Mn}$  and  $I_{IV}^{Mn}$ , or in the case when their difference enters and the inaccuracy due to these terms cancels out. Relying on the correlation between the calculated and experimental optical energies we can try to refine the values of  $I_{III}^{Mn}$  and  $I_{IV}^{Mn}$ , which determination *in-crystal* presents difficulties due to non-closed 3d shell of  $Mn^{3+}$  ion. Indeed, expecting correlation between the calculated optical energy of the fundamental transition of CT character  $O(2p) - Mn(3d)$ ,  $E_{opt} = I^O - I_{III}^{Mn} + S[Mn^{3+}, O^{2-}]_{opt} = -13.91 - 30.63 + 50.15 = 5.61$  eV (see Table V, transition 5) with the broad optical band observed in the  $\epsilon_2$  function near 4.75 eV (dotted curve 3 in Figure 5, (b)) we can refine the third *in-crystal* ionization potential of manganese as  $I_{III}^{Mn*} = 31.49$  eV and, correspondingly,  $I_{IV}^{Mn*} = 48.27$  eV. Using these corrected values we recalculated the energies of transitions 2 and 3 in Table V associated with the CT transitions of  $O^-$  and  $Mn^{4+}$  self-trapped holes and obtained close values of optical energies  $E_{opt} = 2.29$  eV and  $E_{opt} = 2.12$  eV, respectively. These corrected values for the optical CT transition energies are presented in brackets in Table V for transitions 2 and 3. We suggest that these CT transitions  $Mn^{4+} + O^{2-} \Rightarrow Mn^{3+} + O^-$  and  $O^- + Mn^{3+} \Rightarrow O^{2-} + Mn^{4+}$  associated with the hole transfer along a chain  $Mn^{4+} - O^{2-} - Mn^{3+}$  could be responsible for the band around 2.3 eV in the optical conductivity spectrum (the related band in the  $\epsilon_2$  spectrum has maximum energy 1.93 eV) of as-grown non-stoichiometric  $LaMnO_3$  crystal. If the band is assigned so, the net oscillator strength of this band  $f_i = 0.51$  (see Table IV) will be dependent on the concentration of the localized holes as  $f_i = f_{CT}/x$  providing an estimate of oscillator strength for the CT transition,  $f_{CT}$ . The typical value of  $x \sim 0.1$  for as-grown  $LaMnO_3$  crystal gives the estimate for the oscillator strength consistent with the transition of CT-type.

The negative value of the thermal energy,  $E_{th} = -0.75$  eV, for transition 2 from Table V indicates on more thermally stable state of the  $Mn^{4+}$  hole compared to the  $O^-$  hole state, in accordance with our results for the thermal energies of the holes formation  $E_{th}^\alpha$  (Table III, (a)) based on preliminary estimates for the fourth *in-crystal* ionization potential of manganese ion. Using now the refined value of  $I_{IV}^{Mn} = 48.27$  eV, deduced from the comparison between the calculated and experimental optical energies, we derive the thermal energies for transitions 2 and 3 of 0.12 and -0.12 eV, respectively. This result reinforces our arguments made above that the electronic hole can be thermally stable on both transition metal cation and oxygen anion in  $LaMnO_3$  crystal.

In accordance with our shell model calculations the intervalence CT transition  $Mn^{4+} + Mn^{3+} \Rightarrow Mn^{3+} + Mn^{4+}$  is predicted to have the optical energy  $E_{opt} = 1.33$  eV (Table V, transition 1), compared with the energy of the optical gap in  $LaMnO_3$ , and it is not observable in as-grown pure crystal.

Due to doping effect the optical spectra in CMR manganese oxides show striking changes over a wide photon region (0 to 6 eV). In  $La_{1-x}Sr_xMnO_3$  system, with increasing doping concentration from  $x = 0$  to 0.3 at  $T = 9$  K [26], the optical conductivity bands around 2.3 and 5 eV shift by more than 0.5 eV to lower energies. We have analyzed the low-energy  $\epsilon_2$  function in a slightly doped  $La_{7/8}Sr_{1/8}MnO_3$  compound [28], and found it to be well described by the Lorentzian with the maximum at 1.32 eV and the half-width of 0.61 eV, as presented in Figure 6. We would like to emphasize that the maximum position of this band and its half-width are also in a good correlation with the formula describing transition of CT character (see Eq. 10): from  $\Delta W \simeq 0.61$  eV we obtain  $h\nu_{max} \simeq 1.34$  eV, which matches well the maximum position experimentally observed. It would appear reasonable to suggest that this band is due to the same origin as the band at  $\epsilon_2 = 1.93$  eV in pure  $LaMnO_3$  compound, assigned due to transitions 2 and 3, Table V, and shifted by about 0.5 eV to lower energies due to the hole interaction effect in CMR systems. Using this line of reasoning, we can also suggest that the 0.6 eV band [18, 26] in optical conductivity of CMR compounds is due to the intervalence CT transition  $Mn^{4+} + Mn^{3+} \Rightarrow Mn^{3+} + Mn^{4+}$ , and associated with photo-induced hopping conductivity of  $Mn^{4+}$  localized holes, with the consistent value of hopping conductivity activation energy of  $\sim 0.15$  eV measured in the adiabatic temperature limit [29, 30].

The results given are based on the shell model parameters (Table I,(a)), which were fitted to give good values for both the dielectric constants and the transverse optic modes. When we use the second set of the shell model parameters, determined primarily using the oxide structures  $MnO$ ,  $LaMnO_3$ , and  $Ca_2MnO_4$  [20] (Table 1, (c)), the resulting energies are very similar for the low energy optical CT transition band near 2.3 eV, but the predicted energies are about 1.5 eV higher for  $\sim 5$  eV optical band.

## V. CONCLUSIONS

In this paper we explore the role of electronic and ionic polarisation energies in the physics of the CMR materials. In particular, we examine energies associated with localized holes of  $Mn^{4+}$  and  $O^-$  in the lattice of the "parent"  $LaMnO_3$  compound. Our calculations are made for the idealized cubic perovskite  $LaMnO_3$  structure, which is relevant to the non-magnetic quasicubic perovskite structure experimentally observed at high temperatures  $T \geq 400$  K  $> T_N \simeq 140$  K. To estimate the polarisation energy terms we use a fully-ionic shell model. The shell model parameters we derive satisfy the equilibrium conditions for the quasicubic perovskite structure of  $LaMnO_3$  and agree well with experimental

values of the static and high-frequency dielectric constants as well as transverse optical phonons.

As a result of our shell model calculations we find that, from one side, there is a huge difference between the hole relaxation energies on the oxygen and manganese sites which indicates on the strong electron-phonon interaction in the case of the hole localized at the O-site. From the other side, the difference, which we find between the thermal energies of  $\text{Mn}^{4+}$  and  $\text{O}^-$  holes is too small. This means, in fact, we should consider seriously the likelihood that the electronic hole in  $\text{LaMnO}_3$  is localized on the manganese, or on both oxygen anion and transition metal cation, rather than on the oxygen ion alone. If so, this system would be like many other transition metal oxides.

Assuming that holes in  $\text{LaMnO}_3$  crystal can localize in either or in both Mn and O sublattices, we estimate the main associated optical CT transition energies, which we relate to the experimentally observed optical conductivity spectra. Applying the Mott-Littleton approach we estimate the CT transition energies within a Born-Hyber cycle using the *in-crystal* ionization potentials for the ions in  $\text{LaMnO}_3$  crystal obtained in our consideration of the experimental photoemission spectra.

Our analysis allows us to suggest a new interpretation of the main bands in the optical conductivity spectrum at  $\sim 2.3, 5$  eV. We suggest that the band at  $\sim 5$  eV is associated with the fundamental  $\text{O}(2p)\text{-Mn}(3d)$  transition of CT character, whereas the band at  $\sim 2.3$  eV is rather associated with the presence of  $\text{Mn}^{4+}$  and/or  $\text{O}^-$  self-trapped holes in non-stoichiometric  $\text{LaMnO}_3$  compound.

To summarize, we believe that the results of this work demonstrate the applicability and usefulness of the shell model approach to preliminary modeling of polaron-related features in complex oxides such as CMR materials, and hope that they will stimulate further theoretical and experimental studies of the character and properties of hole states in these materials.

### Acknowledgments

The authors thank Dr. J. Gale for making available General Utility Lattice Program (GULP) used in the present calculations. We are greatly appreciate Y. Tokura and T. Arima for providing us the original reflectivity spectra in  $\text{LaMnO}_3$ . We thank to F. Mayr and coauthors for the permission to reproduce their experimental data. We would also like to thank W.C. Mackrodt and A. Ionov for useful information. We are grateful to R.W. Grimes and D.J. Bradfield for fruitful discussions and for making available to us one set of interatomic potentials. We are grateful for Royal Society/NATO support of the visit to University College London of one of us (N. Kovaleva).

- 
- [1] A. J. Millis, R. Mueller and B. I. Shraiman, *Phys. Rev. B* **54** 5405 (1996).
  - [2] H. L. Ju, H. C. Sohn, and Kannan M. Krishnan, *Phys. Rev. Lett.* **79** 3230 (1997).
  - [3] G. D. Watkins, *Inst. Phys. Conf. Ser.* **31** 95 (1977); K. M. Lee, Le Si Dang and G. D. Watkins, *Solid State Communications* **35** 527 (1980); D. Jeon, H. P. Gislason and G. D. Watkins, *Mat. Sci. Forum* **10-12** 851 (1986).
  - [4] J. H. Harding and A. M. Stoneham, *J. Phys. C* **15** 4649 (1982).
  - [5] B. G. Dick and A. W. Overhauser, *Phys. Rev.* **112** 90 (1958).
  - [6] W. Cochran, *Crit. Rev. Sol. St. Sci.* **2** 1 (1971).
  - [7] A. M. Stoneham, M. J. L. Sangster and P. W. Tasker, *Phil. Mag. B* **44** 603 (1981).
  - [8] D. G. Muxworthy and C. R. A. Catlow, *Phil. Mag. B* **37** 63 (1978).
  - [9] R. Englman, *The Jahn-Teller Effect in Molecules and Crystals*, ed. by Wiley-Interscience (1972).
  - [10] A. L. Shluger and A. M. Stoneham, *J. Phys.: Condens. Matter* **5** 3049 (1993).
  - [11] N. F. Mott and M. J. Littleton, *Trans. Faraday Soc.* **34** 485 1938; C. R. A. Catlow and W. C. Mackrodt, *Computer Simulations of Solids*, ed. by Berlin, Springer (1982); These techniques has been reviewed in a special issue: C. R. A. Catlow and A. M. Stoneham, *J. Chem. Soc. Faraday Trans. II* **85** (1989).
  - [12] J. D. Gale, *J. Chem. Soc. Faraday Trans.* **93** 69 (1992).
  - [13] C. R. A. Catlow and A. M. Stoneham, *J. Phys. C* **16** 4321 (1983).
  - [14] C. R. A. Catlow, W. C. Mackrodt, M. J. Norgett and A. M. Stoneham, *Phil. Mag.* **35** 177 (1977).
  - [15] T. Arima and Y. Tokura, *J. Phys. Soc. Jpn.* **64** 2488 (1995).
  - [16] T. Arima and Y. Tokura, *Private communication*.
  - [17] M. S. Islam, M. Cherry and C. R. A. Catlow, *J. Sol. St. Chem.* **124** 230 (1996).
  - [18] A. V. Boris, N. N. Kovaleva, A. V. Bazhenov et al., *Phys. Rev. B* **59** R697 (1999).
  - [19] A. V. Boris, N. N. Kovaleva, A. V. Bazhenov et al., *J. Appl. Phys.* **81** 5756 (1997).
  - [20] R. Grimes and D. Bradfield, *Private communication*.
  - [21] W. E. Pickett and D. J. Singh, *Phys. Rev. B* **53** 1146 (1996).
  - [22] T. Saitoh, *Phys. Rev. B* **56** 8836 (1997).
  - [23] J. H. Park, C. T. Chen, S- W. Cheong et al., *Phys. Rev. Lett.* **76** 4215 (1996).

TABLE I: Potential parameters for short-range interactions in  $\text{LaMnO}_3$  ( $Pm\bar{3}m$ ). (a) - elaborated in the present work; (b) - from M.S. Islam *et al.* [17]; (c) - from R. Grimes [20] for  $\text{Mn}^{3+}$  and  $\text{Mn}^{4+}$  different valent states;  $r_{cutoff} = 20\text{\AA}$ .

	A(eV)	$\rho(\text{\AA})$	C(eV $\cdot\text{\AA}^{-6}$ )	Y( e )	k (eV $\cdot\text{\AA}^{-2}$ )
(a) $\text{La}^{3+}:\text{O}^{2-}$	1516.3	0.3639	0.00		
$\text{Mn}^{3+}:\text{O}^{2-}$	1235.9	0.31525	0.00		
$\text{O}^{2-}:\text{O}^{2-}$	22764.3	0.1490	20.37	-2.48	16.8
(b) $\text{La}^{3+}:\text{O}^{2-}$	1516.3	0.3525	0.00		
$\text{Mn}^{3+}:\text{O}^{2-}$	1235.9	0.3281	0.00		
$\text{O}^{2-}:\text{O}^{2-}$	22764.3	0.1490	43.00		
(c) $\text{La}^{3+}:\text{O}^{2-}$	2088.79	0.3460	23.25		
$\text{Mn}^{3+}:\text{O}^{2-}$	922.83	0.3389	0.00		
$\text{Mn}^{4+}:\text{O}^{2-}$	1386.14	0.3140	0.00		
$\text{O}^{2-}:\text{O}^{2-}$	9547.96	.2192	32.00	-2.04	6.3

TABLE II: Crystal properties of  $\text{LaMnO}_3$  ( $Pm\bar{3}m$ ) calculated using the shell model potentials (Table I) and compared with experimental data.

	Lattice const. $a_0$ , ( $\text{\AA}$ )	Cohesive energy $E_{lat}$ , (eV)	$\epsilon_0$	$\epsilon_\infty$	$\omega_{TO_1}$	$\omega_{TO_2}$	$\omega_{TO_3}$
					(cm $^{-1}$ )		
Exp.	3.889		$18 \pm 2$ [15]	4.9 [15]	172 [15]	360 [15]	560 [15]
Calc. (a)	3.889	-140.52	15.6	4.9	172	308	513
Calc. (b)	3.904	-139.12	56.17				
Calc. (c)	3.906	-139.58	14.1	4.6	156	252	368

- [24] D. R. Lide, *Handbook of Chemistry and Physics*, 73<sup>rd</sup> edition (1993).
- [25] J. H. Harding and N. C. Pyper, *Phil. Mag. Lett.* **71** 113 (1995).
- [26] Y. Okimoto, T. Katsufuji, T. Ishikawa et al., *Phys. Rev. B* **55** 4206 (1997).
- [27] H. J. Lee, J. H. Jung, Y. S. Lee et al., *Phys. Rev. B* **60** 5251 (1999).
- [28] F. Mayr, C. Hartinger, M. Paraskevopoulos et al., *Phys. Rev. B* **62** 15673 (2000).
- [29] M. Jaime, M. B. Salamon, M. Rubinstein et al., *Phys. Rev. B* **54** 11914 (1996).
- [30] A. Machida, Y. Morimoto, and A. Nakamura, *Phys. Rev. B* **58** 12540 (1998); *Phys. Rev. B* **58** R4281 (1998).
- [31] I. Solovyev, N. Hamada and K. Terakura, *Phys. Rev. B* **53** 7158 (1996).
- [32] K. Takenaka, Y. Sawaki, R. Shiozaki, and S. Sugai, *Phys. Rev. B* **62** 13864 (2000).
- [33] N. S. Hush, *Prog. Inorg. Chem.* **8** 391 (1967).

TABLE III: Formation and polarisation energies for localized holes in LaMnO<sub>3</sub>: (a) - for the pair potentials explored in this work; (c) - for the pair potentials from R. Grimes [20] for Mn<sup>3+</sup> and Mn<sup>4+</sup> different valent states.

$\alpha$ -hole	$E_h^\alpha(opt)$	$E_h^\alpha(th)$	$I^\alpha(E_{IV}^\alpha)$	$S_{opt}^\alpha$	$S_{th}^\alpha$	$U_M^\alpha$	$R_{opt}^\alpha$	$\Delta R_{th}^\alpha$	$E_{PES}^\alpha$
(a) Mn <sup>4+</sup>	2.56	1.73	47.41 (51.20)	-44.85	-45.68	-38.3	-6.55	-0.83	1.2
O <sup>-</sup>	4.86	2.48	-13.91	18.77	16.39	22.1	- 3.33	-2.38	3.5
La <sup>4+</sup>	18.36	17.63	49.45 (49.45)	-31.09	-31.82	-27.4	-3.68	-0.73	17.0
(c) Mn <sup>4+</sup>	2.62	1.95	46.83 (51.20)	-44.27	-44.94	-38.1	-6.17	-0.67	1.2
O <sup>-</sup>	4.92	2.52	-13.82	18.74	16.34	22.0	-3.26	-2.40	3.5
La <sup>4+</sup>	18.42	17.84	49.45 (49.45)	-31.03	-31.61	-27.4	- 3.63	-0.58	17.0

TABLE IV: Parameters of the imaginary part of the dielectric function  $\epsilon_2$  [15, 16] represented by the sum of Lorentzian shaped bands.

$E_i$ (eV)	$\gamma_i$ (eV)	$\nu_{pi}^2$ (eV <sup>2</sup> )	$f_i$
1.93	1.46	1.895	0.51
4.75	2.0	4.22	0.187
9.07	5.1	12.75	0.155

TABLE V: Calculated optical,  $E_{opt}$ , and thermal,  $E_{th}$ , energies for the main charge-transfer transitions in LaMnO<sub>3</sub>.  $S_{opt}$  and  $S_{th}$  are resultant calculated values of the sum of the defect energies corresponding the charge-transfer process considered.

CT transition	Optical energy $E_{opt}$ , (eV)	Exp. (eV)	Thermal energy, $E_{th}$ , (eV)	$S_{opt}$ (eV)	$S_{th}$ , (eV)
1. Mn <sup>4+</sup> + Mn <sup>3+</sup> $\Rightarrow$ Mn <sup>3+</sup> + Mn <sup>4+</sup>	1.33	-	0.00	-44.35	-45.68
2. O <sup>-</sup> + Mn <sup>3+</sup> $\Rightarrow$ O <sup>2-</sup> + Mn <sup>4+</sup>	1.43 (2.29)	1.93	-0.75 ( 0.12)	-43.50	-45.66
3. Mn <sup>4+</sup> + O <sup>2-</sup> $\Rightarrow$ Mn <sup>3+</sup> + O <sup>-</sup>	2.98 (2.12)	1.93	0.75 (-0.12)	18.62	16.39
4. 2Mn <sup>3+</sup> $\Rightarrow$ Mn <sup>4+</sup> + Mn <sup>2+</sup>	Mn(3d) gap 3.72	3.5[27], 3.2 [32]	2.68	-13.06	-14.10
5. Mn <sup>3+</sup> + O <sup>2-</sup> $\Rightarrow$ Mn <sup>2+</sup> + O <sup>-</sup>	O(2p) - Mn(3d) 5.61 (4.75)	4.75	3.50	50.15	48.04
6. La <sup>3+</sup> + O <sup>2-</sup> $\Rightarrow$ La <sup>2+</sup> + O <sup>-</sup>	O(2p) - La(5d) 8.93	9.07	6.47	42.02	39.56

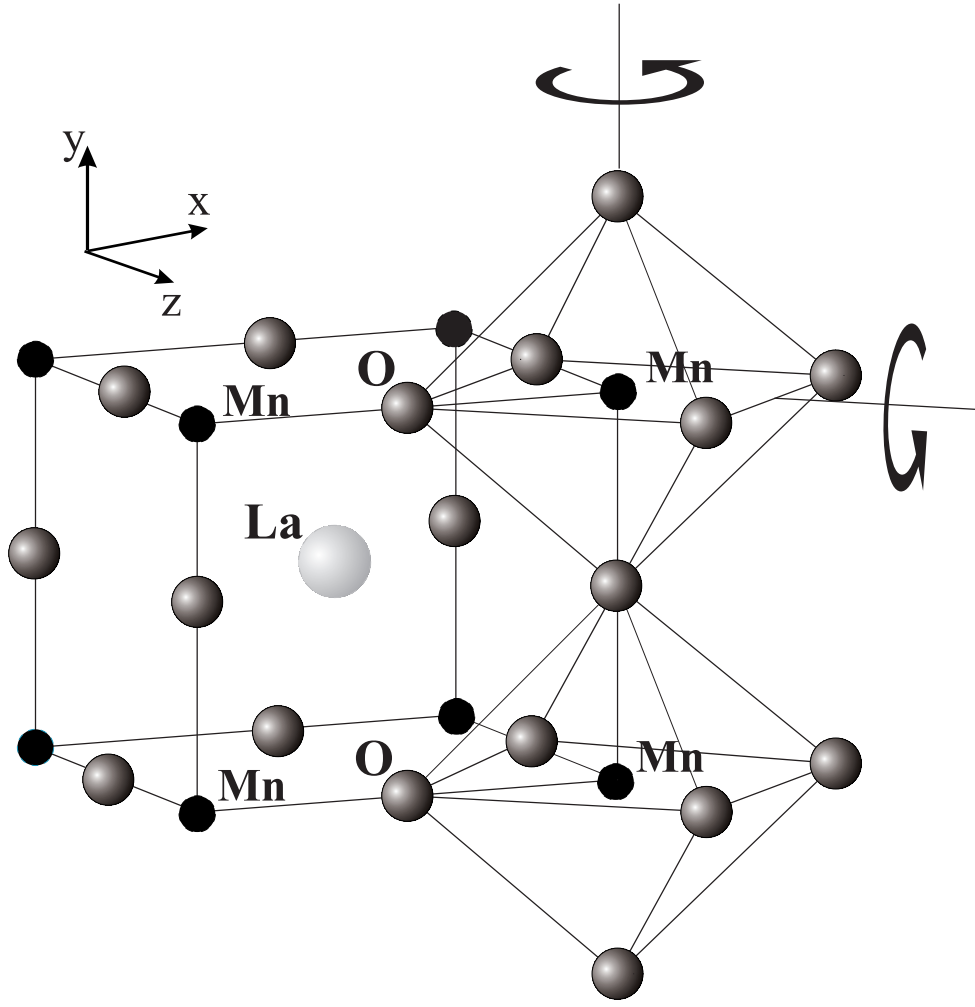


FIG. 1: The idealized cubic perovskite structure ( $Pm\bar{3}m$ ) of  $\text{LaMnO}_3$  crystal. The orthorhombic  $Pnma$  structure can be obtained by two consequent rotations of the  $\text{MnO}_6$  octahedra around the  $[010]$  and  $[101]$  directions.

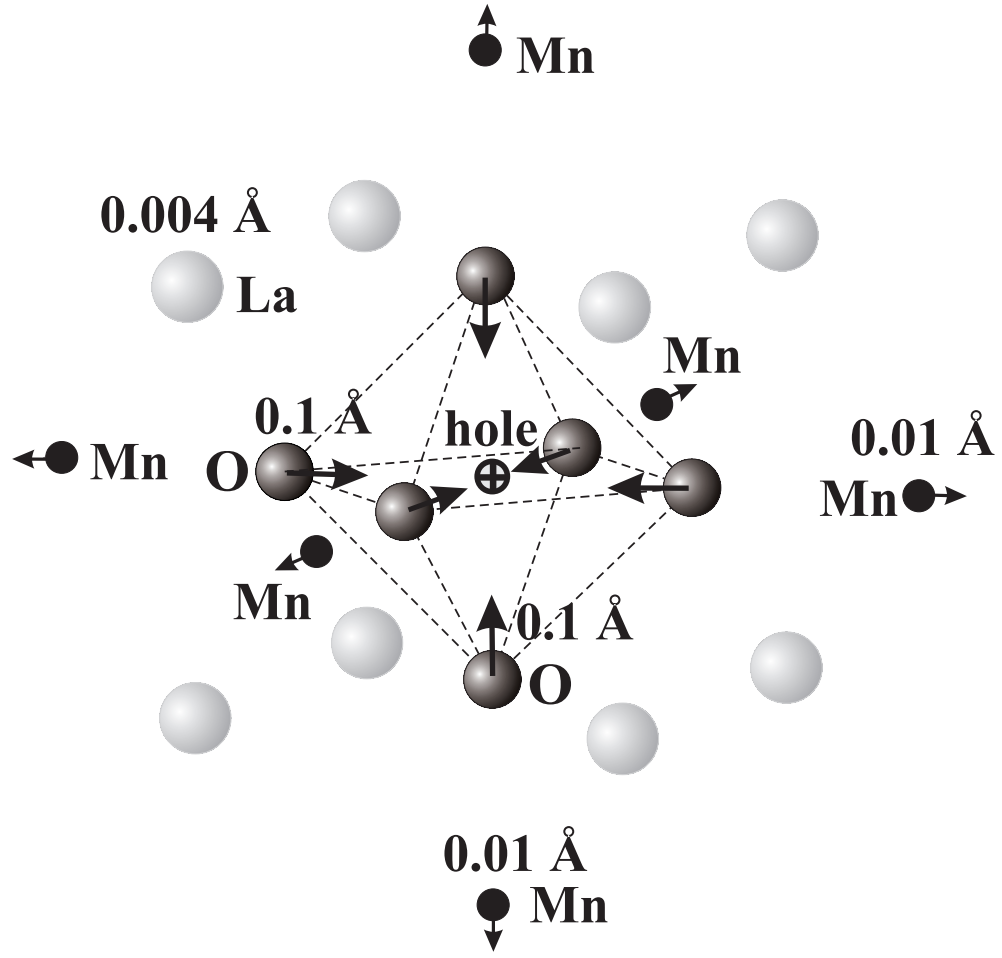


FIG. 2: The core displacements ( $\geq 0.004 \text{ \AA}$ ) of the ions surrounding  $\text{Mn}^{4+}$  electronic hole defect after full relaxation of cores and shells in the  $\text{LaMnO}_3$  lattice.

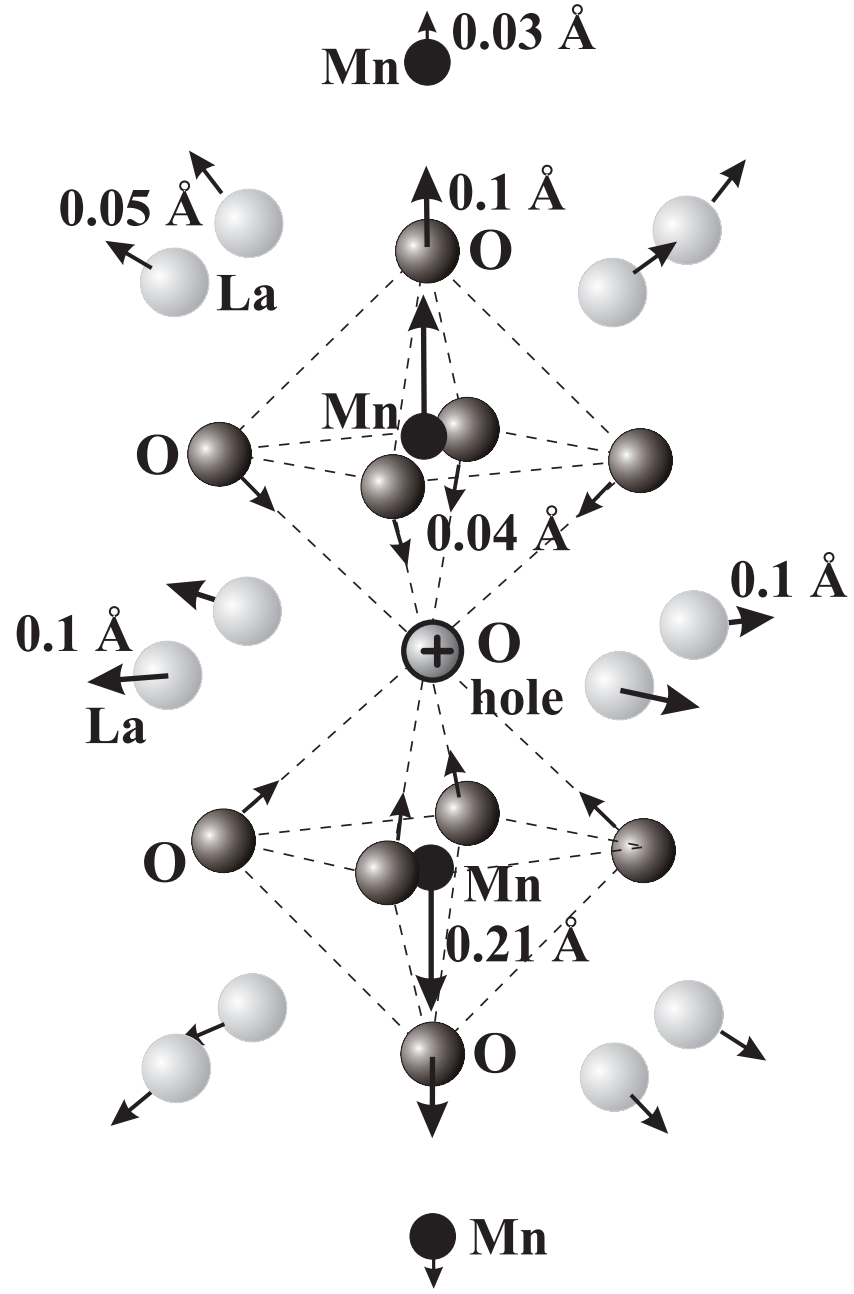


FIG. 3: The core displacements ( $\geq 0.03 \text{ Å}$ ) of the ions surrounding  $O^-$  electronic hole defect after full relaxation of cores and shells in the  $\text{LaMnO}_3$  lattice.

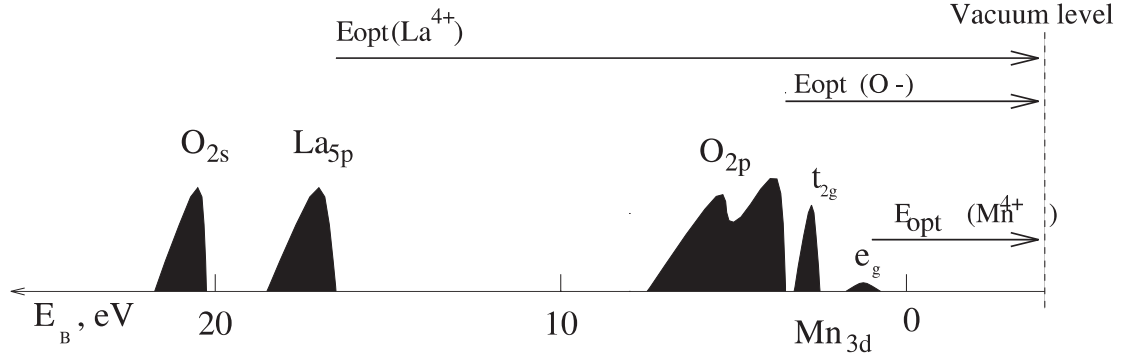


FIG. 4: A schematic representation of the valence band structure of  $\text{LaMnO}_3$  crystal, showing binding energies [22, 23] with respect to the crystal Fermi level  $E_F$ . The electron optical excitation processes to the vacuum level from the  $\text{Mn}(3d)$   $e_g$ ,  $\text{O}(2p)$  and  $\text{La}(5p)$  valence bands are shown by arrows. These optical excitation energies can be compared with experimental photoelectron spectroscopy data [22, 23] and with the calculated values of optical energies,  $E_{opt}$ , for  $\text{Mn}^{4+}$ ,  $\text{O}^-$  and  $\text{La}^{4+}$  hole formation (Table III).



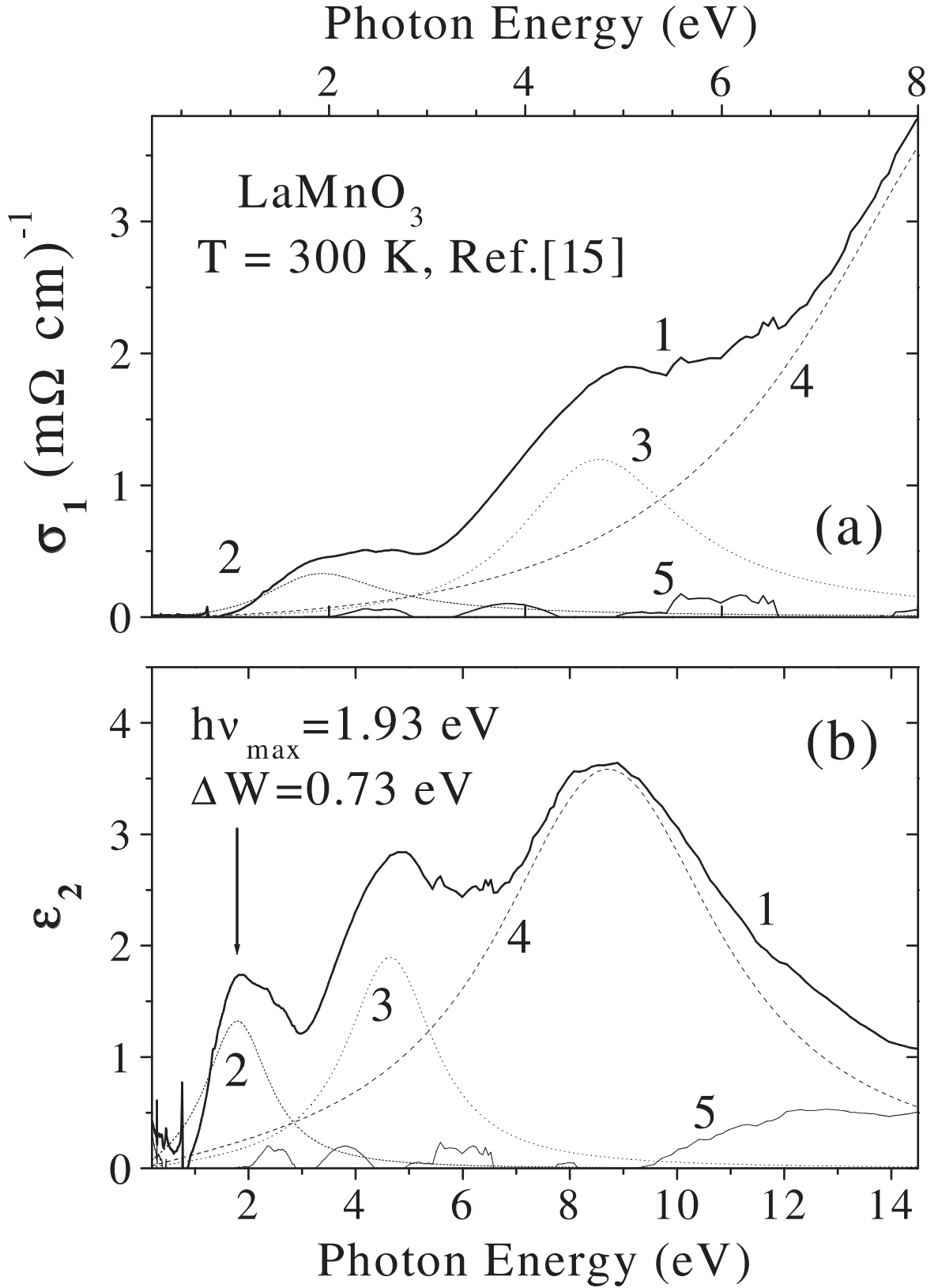


FIG. 5: (a) - The experimental optical conductivity spectrum of LaMnO<sub>3</sub> crystal (solid curve 1, T = 300 K) represented by the contributions from the three Lorentz oscillators in accordance with the dispersion analysis of the imaginary part of the dielectric function  $\epsilon_2$  (b). (b) - The experimental  $\epsilon_2$  spectrum of LaMnO<sub>3</sub> (solid curve 1, T = 300 K) represented by a sum of three main Lorentzian shaped bands: 1.93, 4.75 and 9.07 eV (drawn by short-dashed 2, dotted 3, and long-dashed 4 curves, respectively). The rest of  $\epsilon_2$  spectrum after subtraction of the Lorentzian bands is shown by light line 5. The Lorentzian band parameters are given in the Table IV together with the estimated oscillator strengths  $f_i$ .

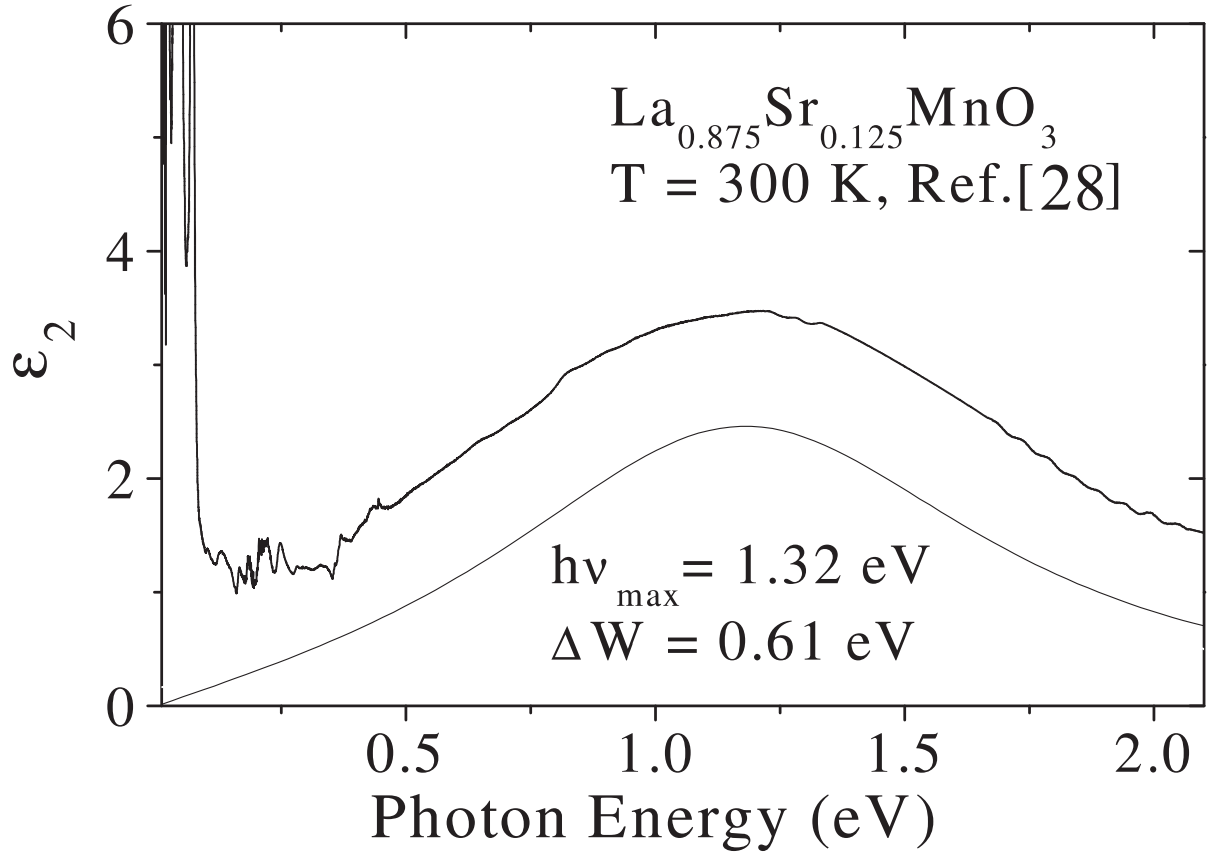


FIG. 6: The experimental  $\epsilon_2$  spectrum of  $\text{La}_{7/8}\text{Sr}_{1/8}\text{MnO}_3$  ([28],  $T = 300 \text{ K}$ ) approximated by the Lorentzian shaped band.